# MATERIALS
## CHEMISTRY
### FRONTIERS

CCS
中国化学会
CHINESE
CHEMICAL
SOCIETY

ICCAS
1956

ROYAL SOCIETY
OF CHEMISTRY | Celebrating
IYPT 2019

**rsc.li/frontiers-materials**

Chinese Chemical Society | ICCAS | ROYAL SOCIETY OF CHEMISTRY

## RESEARCH ARTICLE

Check for updates

# Laser-induced synthesis of ZIF-67: a facile approach for the fabrication of crystalline MOFs with tailored size and geometry†

Erick L. Ribeiro,[abc] Seyyed Ali Davari,[bd] Sheng Hu,[abc] Dibyendu Mukherjee [ID] *[abcd] and Bamin Khomami [ID] *[acd]

Metal organic frameworks (MOFs) are fast emerging as a new class of crystalline hybrid porous materials originating from inorganic (metal) nodes connected by organic linkers. MOFs have gained tremendous interest in the materials science community owing to their versatile functionalities as a result of tailorable chemical activity, porosity, and morphology. In spite of the wide classes of MOF structures synthesized in recent years, rapid yet environmentally friendly fabrication strategies that allow precise morphological and structural control of these frameworks is still challenging. Herein, we report a facile route using high-energy laser ablation synthesis in solution (LASiS) to produce highly crystalline zeolitic imidazolate framework-67 (ZIF-67) structures by ablating Co targets in 2-methylimidazole (Hmim) solutions. Synthesis protocols presented here demonstrate for the first time the ability of LASiS to rationally tailor the sizes and shapes of MOF structures by adjusting solution-phase (reagent concentration and temperature) and laser parameters (ablation time). Our findings indicate that while the average MOF size is controlled by varying the organic linker to LASiS-generated metal ion stoichiometric ratio, tailoring of its morphology occurs *via* precise control of synthesis temperature and duration of ablation. Finally, a mechanistic picture for MOF formation *via* LASiS is presented.

## 1. Introduction

Metal–Organic Frameworks (MOFs) are a class of crystalline and highly porous hybrid materials self-assembled through the coordination of metal ion nodes to organic linkers.[1] Such networked structures are tunable with near infinite possible combinations of nodes and linkers. Furthermore, MOFs are highly permeable with pore sizes ranging from 0.3 to 10 nm[2] that can provide astonishing free volumes (over 90%)[3] and surface areas (over 10 000 m$^2$ g$^{-1}$).[4] Currently, there exist over 20 000 MOFs that have been characterized,[5] and the field is rapidly growing. Thus far, MOFs have been utilized for gas storage,[6] fluid separations,[7] sensing,[8] catalysis,[9] luminescence,[10] and photovoltaics.[11] Recently, a considerable amount of research

efforts have been employed specifically around the synthesis of Zeolitic Imidazolate Frameworks (ZIF), a subclass of MOFs, wherein Co$^{2+}$ or Zn$^{2+}$ ions are bonded through N atoms of imidazole molecules to form unique crystalline-scaffold-like architectures.[12] ZIF morphologies and structures can be tuned by tailoring the synthesis conditions, making it an excellent candidate for a wide range of applications.[13,14] Zinc 2-methylimidazolate (ZIF-8) was first synthesized *via* solvothermal method using dimethylformamide (DMF) as a solvent.[15] Nonetheless, typical solvothermal techniques require high temperature conditions apart from the inherent need for solvent exchange routes to remove the DMF molecules that can remain confined inside the framework pores due to their large sizes when compared to the apertures for the sodalite (SOD) cage.[16] Cobalt 2-methylimidazolate (ZIF-67) is isostructural with ZIF-8, and by virtue of the similar structure and organic linkers, both crystals have an analogous formation mechanism.[17] Furthermore, in recent years various other techniques such as microwave,[18] ultrasound,[19] mechanochemical[20] and numerous other fabrication methodologies have also been extensively studied and developed to synthesize ZIF structures. Nevertheless, despite all these efforts, to date very few sustainable, rapid and yet, high-throughput methods have been reported that can facilitate systematic tailoring of ZIF geometries, crystal structures and sizes in the

*a Department of Chemical & Biomolecular Engineering, University of Tennessee, Knoxville, Tennessee, 37996, USA. E-mail: dmukherj@utk.edu, bkhomami@utk.edu*

*b Nano-BioMaterials Laboratory for Energy, Energetics & Environment (nbml-E³), University of Tennessee, Knoxville, Tennessee, 37996, USA*

*c Sustainable Energy Education & Research Center (SEERC), University of Tennessee, Knoxville, Tennessee, 37996, USA*

*d Department of Mechanical, Aerospace, & Biomedical Engineering, University of Tennessee, Knoxville, Tennessee, 37996, USA*

† Electronic supplementary information (ESI) available. See DOI: 10.1039/c8qm00671g

race for the rapid screening of a wide library of MOFs fabrication with desired engineering functionalities.

In recent years, our group has extensively reported on the design and development of various LASiS-based synthesis routes for the production of diverse classes of complex hetero-nanostructures, including $Co_3O_4$ nanoparticles (NPs)/nanorods (NRs) and single crystal β-$Co(OH)_2$ NPs,[21] Pt-based intermetallic nanocomposites (NCs) and binary/ternary nanoalloys (NAs),[22–27] as well as NCs of $Co_3O_4$ NPs interfaced with reduced/nitrogen-doped graphene oxide,[28] and Al NPs encaged in graphitic shells/carbon matrices.[29] Our rapidly growing volume of work in LASiS-based synthesis routes stems from the unique advantages that the high-energy technique offers, when compared to other conventional wet chemistry routes. Specifically, the extreme temperatures and pressures inside the laser-induced plasma plume facilitate non-equilibrium pathways inside a cavitation bubble initiated by the liquid-confined plasma to nucleate seeding NPs that further grow and evolve *via* subsequent chemical reactions at the bubble-liquid interface once the bubble collapses.[30] Such growth routes also hinder particle coarsening owing to the inherent charge screening effects from the plasma, thereby not requiring the use of unwanted surfactant/ligands that typically contaminate the NP surfaces. Thus, for the particular application of MOF synthesis, one can easily envision the potential use of LASiS in tailoring promising strategies and pathways for the synthesis of active metal NPs encaged in MOF structures that can exhibit unique functionalities even under extreme environments. In fact, previous studies have demonstrated that NPs can either serve as nucleation sites for the growth of MOF crystals, or they can be incorporated into the frameworks of the MOF materials.[31] Such encapsulation strategies can be of paramount importance in active and harsh environments where NPs need to be stabilized within the MOF structures to minimize their aggregations while conserving their properties. To this end, Lu *et al.*,[31] have reported the fabrication of a wide range of NPs confined within ZIF-8 crystals that go onto exhibit active catalytic, magnetic and optical properties. Although LASiS provides a remarkably facile and rapid route for such NP encapsulations in MOF, the first step towards making such designer materials demands a fine control on the size and shape of the parent MOF network produced *via* LASiS. Hence, in this work, we report for the first time LASiS-driven fabrication of ZIF-67 as a model system for MOF designs with tailored size and morphology. Our goal here is to gain a fundamental understanding of the role of solution-phase parameters (*e.g.*, reagents concentration and temperature) along with laser properties in driving the chemistry for the coordination complexation process during LASiS-based MOF formations.

## 2. Experimental

### LASiS based synthesis

All chemicals and precursors were purchased from Sigma-Aldrich. Cobalt pellets were obtained from Kurt J. Lesker (99.95% purity, 1/4″ diameter × 1/4″ height). LASiS experiment was performed in an in-house built laser ablation cell equipped with an injection unit for supplying chemicals and precursors as well as a thermocouple for temperature control as described in detail in our earlier work. For the synthesis of ZIF-67 structures, the desired amount (60, 120, 180 and 240 mg) of 2-methylimidazole (Hmim) was dissolved in 6 mL of potassium hydroxide solution (3 mol $L^{-1}$ KOH in deionized water) before transferring into the LASiS cell through the injection unit. The solutions were maintained at 65 °C during for the entire experiment. The target metal was ablated using an unfocused 1064 nm pulsed Nd-YAG laser (330 mJ per pulse, 10 Hz), while being rotated by a stepper motor at a uniform speed of 0.3 rpm, for different ablation times (2–5 min). To ensure complete crystallization of the MOFs, the suspension was maintained at 65 °C for 12 hours. The products were then collected by centrifuging at 4700 rpm for 15 min and decanted after washing two with methanol. For the sake of comparison, the same procedure was repeated at a different synthesis temperature.

### Characterizations

Scanning electron microscopy (SEM) images were obtained using a Philips XL-30ESEM equipped with an energy dispersive X-ray spectroscopy. Inductively coupled plasma optical emission spectroscopy (ICP-OES) (Perkin Elmer, Optima 4300 DV) was used to measure the Co concentrations for each ablation time, where $CoCl_2$ salts were used as standards for the calibrations. X-ray diffraction (XRD) was carried out on a Phillips X'Pert-Pro diffractometer equipped with a Cu Kα source at 45 kV and 40 mA. Fourier transformed infrared (FTIR) spectrum was recorded using a Nicolet 6700 FT-IR Spectrometer in the wavenumber range of 400 to 3000 $cm^{-1}$. Thermogravimetric analysis (TGA) was carried out under a nitrogen atmosphere using a Perkin Elmer Thermal Analyzer at a heating rate of 5 °C $min^{-1}$.

## 3. Results and discussion

We report here the development of a general methodology to synthesize MOF structures using LASiS. Specifically, we present the results that depict our approach in understanding the influence of reaction parameters along with laser properties on the final MOF size and geometry. In doing so, we have studied the synthesis of ZIF-67 under a variety of experimental conditions for LASiS. Firstly, X-ray diffraction (XRD) analysis was carried out in order to investigate the purity and crystallinity of the as-synthesized structures. To this end, Fig. 1a shows the XRD patterns for the products synthesized using 2 min of ablation with 40 mg $cm^{-3}$ of Hmim. The diffraction patterns obtained are clearly indexed to the standard ZIF-67 crystal structure patterns. Thus, the formation of a pure-phase material is confirmed *via* comparisons with the simulated patterns. FTIR spectra for the products synthesized under the aforementioned conditions are indicated in Fig. 1b. The spectral bands observed at 687 $cm^{-1}$ and 754 $cm^{-1}$ are ascribed to the out-of-plane bending of the Hmim ring, whereas the peaks around 900 $cm^{-1}$ and 1350 $cm^{-1}$ are assigned to the in-plane bending. It is well-known that the
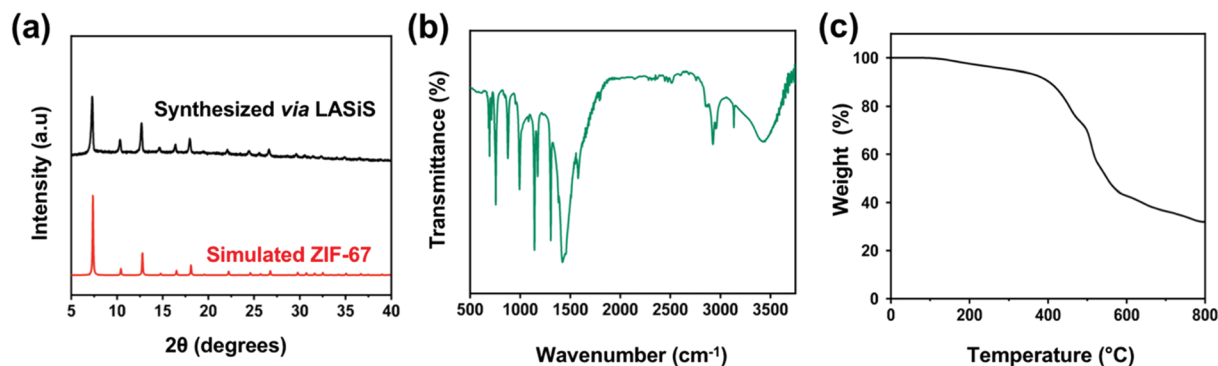
Fig. 1 (a) XRD pattern (b) FTIR spectra and (c) TGA thermographs of the frameworks synthesized under 2 min ablation and Hmim concentration of 40 mg cm$^{-3}$.

band at 1678 cm$^{-1}$ corresponds to the bending of the N–H in the Hmim molecule, while the peak at 1581 cm$^{-1}$ is associated to the N–H vibrations in the same structure. Added to this, intense peak observed at 1524 cm$^{-1}$ is attributed to the stretching of the Hmim aromatic ring and the bands at 2930 and 3124 cm$^{-1}$ arise from the Hmim aliphatic and aromatic C–H stretching, respectively. Finally, thermogravimetric analysis (TGA) for the synthesized ZIF sample, shown in Fig. 1c, clearly indicates the high thermal stability of these frameworks up to ∼380 °C, where a weight loss of approximately 62.5% is observed.

This can be associated to the decomposition of the Hmim molecules in the ZIF-67 crystals, wherein the initial weight loss is attributed to the removal of water and free organic linker molecules that remain trapped inside the framework pores.

## A mechanistic picture of the laser induced MOF formation

Having verified the structural characteristics of the ZIF-67 crystals synthesized here, we turn our attention to elucidate the role of LASiS parameters in tailoring the synthesis of these MOF materials. Herein, we present a detailed mechanistic picture for the governing reaction pathways initiated by the high-energy laser ablation that give rise to the framework formations. To this end, the chemical stages of ZIF-67 production *via* LASiS are illustrated in Fig. 2. Initially, the pulsed laser beam thermally vaporizes the metal target in solution to generate a plasma plume with extremely elevated temperatures and pressures (∼10$^3$ K and 10$^6$ Pa, respectively), which is confined by the surrounding liquid environment. The extreme conditions inside the plasma plume leads to supersaturation of vaporized metal monomers that ultimately nucleate to form the seeding Co
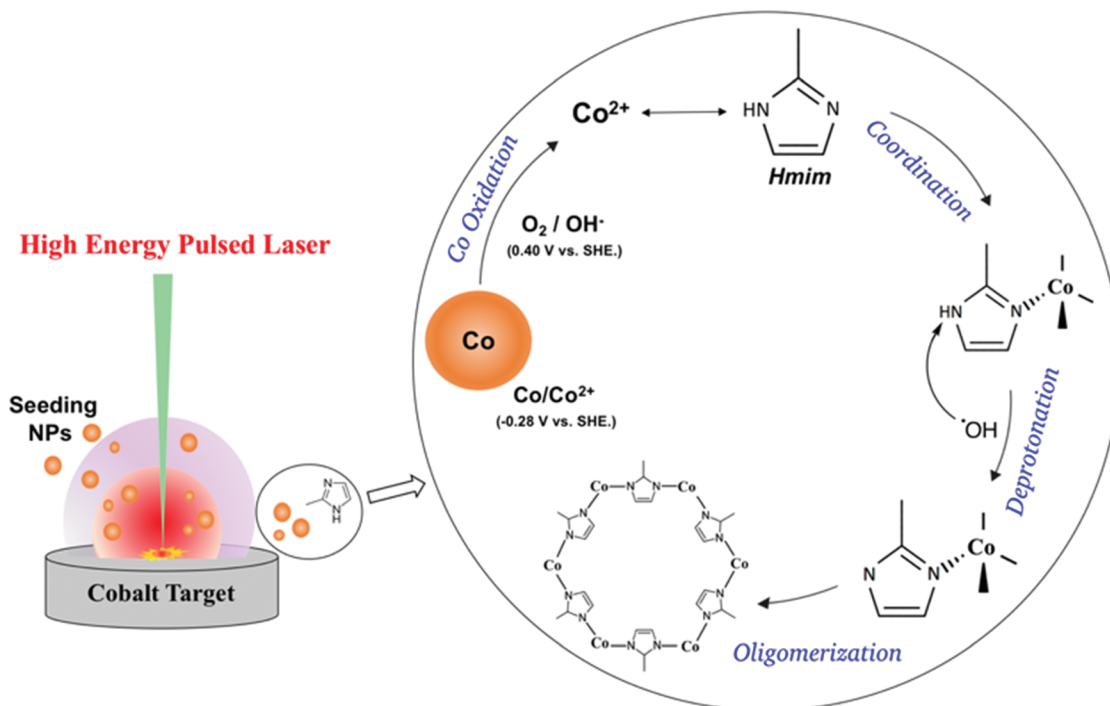


Fig. 2 Proposed mechanism for the laser-induced ZIF-67 formation.

nanoparticles (NPs) within an oscillating cavitation bubble formed by the shock waves emanating from the expanding plasma plume. This bubble ultimately collapses causing the NPs to undergo a collisional quenching that subsequently leads to reactions with the solution-phase species at the bubble–liquid interface. During our synthesis technique, the metallic Co NPs nucleated from the ablation process are rapidly oxidized by the species present in the aqueous solution resulting in the production of $Co^{2+}$ ions driven by the relative redox potentials: ($O_2/OH^-$ 0.40 V $vs.$ SHE)/($Co/Co^{2+}$ −0.28 V $vs.$ SHE).[21] In a previous study, Ozturk $et\ al.$[32] had proposed the reaction pathways that lead to the formation of ZIF-67 structures. According to this proposed mechanism, MOF formations consisted of three main reaction steps: (1) coordination of $Co^{2+}$ centers by the Hmim molecules, (2) deprotonation of Hmim, and finally (3) oligomerization by bridging separated $Co^{2+}$ centers $via$ the deprotonated Hmim. Correspondingly, in our methodology, once the initiation of the $Co^{2+}$ ion generations is caused by the oxidation of the LASiS-produced metallic Co NPs, the subsequent solution-phase reaction steps follow the proposed mechanisms as described by Ozturk $et\ al.$ Thus, it is reasonable to suggest that immediately upon the formation of $Co^{2+}$, the Hmim molecules present in the solution initiate the coordination of these metal centers giving rise to the deprotonation and subsequently oligomerization that leads to the formation of the framework structures. The elevated hydroxyl concentrations in the system associated to the initial KOH is necessary considering that the Hmim deprotonation is not feasible at a lower pH due to its high $pK_a$ values ($pK_a$(Hmim) = 14.2).[13]

### Effect of organic linker concentration along with ablation time

A common observation in most previous MOF formation studies have been the obvious role played by the stoichiometric ratio of the organic linkers to metal ions in tailoring the different structural architectures in MOF materials.[17,18,32,33] While the linker concentration in our system can be adjusted by simply varying the quantity of Hmim initially injected into the reactor cell, the metal ion concentrations can be accurately regulated by varying the ablation time for a constant laser pulse energy, as shown by the ICP-OES measurements presented in Fig. S1 (ESI†). Based on this approach, the molar ratios of organic linker (Hmim) to metal ion ($Co^{2+}$) for each of the LASiS experimental conditions used in this study are represented in Fig. 3. The coloured elliptical forms display the respective values/ranges of the Hmim : Co molar ratios obtained for the various combinations of linker concentrations and ablation times. Here, the ratios within a range of 15 units are grouped under the same area. Guided by these ratio maps, the final morphologies of the ZIF frameworks are analysed using Scanning Electron Microscopy (SEM), as depicted in Fig. 4a. The images reveal the well-known cubic crystalline geometry of ZIF-67 with a broad size distribution ranging from several ~10–100 nm, depending on the specific combination of the linker concentration and ablation time used.

The SEM micrographs clearly show a decreasing trend in the average framework sizes when the concentration of Hmim is increased while maintaining the ablation time constant.
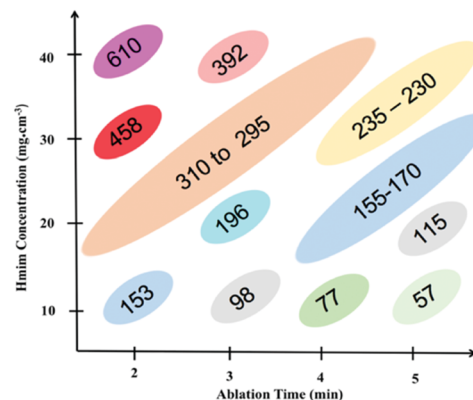


Fig. 3 Stoichiometric ratio of Hmim to cobalt for the various experimental conditions used.

For instance, for the 5 min ablation time, the synthesized ZIF structures reach dimensions close to ~300–800 nm range for the lowest Hmim concentration. On the other hand, the frameworks are observed to reach a range of ~75–200 nm at the highest Hmim concentrations. A more detailed and quantitative size distributions for the aforesaid experimental conditions are presented in Fig. 4b. These histograms indicate good agreements with the visual inspection provided by the SEM images in Fig. 4a. In general, the most accepted models for the formation of crystalline structures are based on the hypothesis that these phenomena occur $via$ two separated events: nucleation and growth. Specifically, LaMer and coworkers[34,35] have proposed the concept of burst nucleation, which has been widely applied for the study of crystal formation since its first publication in 1950. According to LaMer's model, the nucleation events take place immediately when the concentration of monomers in the system reaches a critical supersaturation value ($C_{max}$). At this stage, the burst nucleation simultaneously forms a population of nuclei, brings the monomers concentration below the supersaturation condition and finally, ends the nucleation phenomena.[36] The second stage is characterized by the growth of the just-formed critical nuclei $via$ diffusion of monomers. Sugimoto $et\ al.$[37,38] had later on developed a simple analysis that extended LaMer's model; the proposed modeling suggests a linear relationship between the nuclei population ($p_T$) and the monomers supply rate ($Q$). For our system, $Q$ can be interpreted in terms of the deprotonation rate, which is the key step in the formation of monomers. In summary, for our MOF systems we observe two distinct growth processes: (1) increase in the average MOF sizes with increasing ablation time for a given Hmim concentration, and (2) decrease in the average sizes of MOFs with increasing Hmim concentrations for a given ablation time. These observations can be rationalized taking into consideration the aforementioned LaMer's and Sugimoto's models in conjunction with the relative stoichiometric ratios of Hmim : $Co^{2+}$. More specifically, for a given ablation time, a higher initial Hmim concentrations would facilitate a greater number of $Co^{2+}$ being coordinated by the Hmim molecules. In turn, larger existence of these coordination centers can be associated with an increase in the Hmim deprotonation
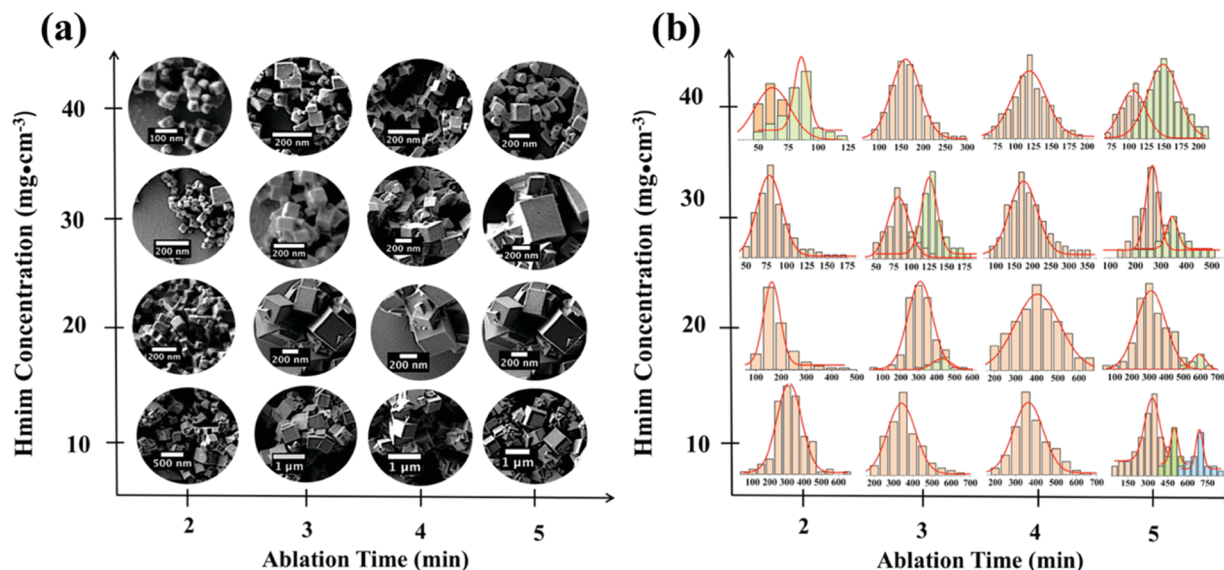
**Fig. 4** (a) SEM micrographs and (b) framework size distribution for the various experimental conditions used.

rates which promotes higher nuclei formations as predicted by Sugimoto's model. This tendency to promote higher nuclei formations generates larger concentrations of MOFs with relatively limited sizes; particularly, if one takes into consideration that a vast majority of the Hmim/Co materials will form individual nuclei rather than participate in the growth stage. On the other hand, as the ablation time increases, a more detailed analysis of the system reveals a more complex process since the increase in the $Co^{2+}$ concentration with the ablation time does not take place instantly, but rather, in a step-wise fashion. Herein, we hypothesize that this systematic production of the $Co^{2+}$ with the ablation time induces the nucleation burst to take place more than once, generating multiple populations of MOFs that undergo growth processes during different periods of time giving rise to, in certain cases, multimodal size distributions (Fig. 4b). To further explain this phenomenon, Fig. S2a (ESI†) provides an illustration of our proposed mechanism based on the LaMer's model wherein the increase in monomer concentrations in the system over time due to the ongoing deprotonation combined with constant $Co^{2+}$ supply (laser pulses) results in their maximum value ($C_{max}$) that initiates the first nucleation event (Nucleation Event I) to generate a nuclei population ($P_1$) in the system. At this stage, the monomer concentration drops below $C_{max}$ and beyond this point, $P_1$ undergoes diffusion-driven growth processes that continuously increase the MOF sizes over time. One needs to bear in mind that during this phase, the formation of monomers is not completely suppressed. On the contrary, the continuous increase of $Co^{2+}$ concentrations in the system due to the continuing pulsed-laser ablation in conjunction with the ongoing Hmim deprotonation, enhances the monomer formation processes, thereby elevating the resulting concentrations of these species in the system. Once the system reaches the critical supersaturation conditions for the second time, Nucleation Event II takes place giving rise to another nuclei population of $P_2$. Herein, $P_2$ will not partake in the subsequent growth processes, albeit the earlier onset of the

$P_1$ population growth would naturally imply that at this later stage the average framework sizes for $P_1$ would have grown to be larger than that for $P_2$. One can imagine that this sequence of events can take place $N$ times, until the monomers formation finally is suppressed by the termination of the $Co^{2+}$ species supply in the system associated with the cease of ablation processes. Hence one could plausibly argue that in many cases, the appearance of multimodal MOF size distributions are more probable to occur during the transition stages between two unimodal MOF size distributions. Thus, as ablation time increases for a given concentration of organic linkers, we increasingly observe the appearance of secondary peak sizes as the overall MOF size distributions shift to higher peak modal values.

Fig. 4b clearly shows the occurrence of bimodal (*e.g.*, 40 mg cm$^{-3}$/2 min and 30 mg cm$^{-3}$/3 min cases) and even trimodal size distributions (*e.g.*, 10 mg cm$^{-3}$/5 min) under certain synthesis conditions. Thus, these observations can be ascribed to the presence of MOF structures from $N$ different populations with different size distributions and peak modal sizes. A tentative schematic presented in Fig. S2b (ESI†) helps visualize the expected evolution of the MOF size distributions in the system as per the aforementioned proposed mechanistic picture. One can easily notice here that the increasing ablation times promote the emergence of distinct modal peaks in the overall MOF population size distributions. Nevertheless, at longer ablation times, it can be expected that two or more of these modal peaks will merge to form one single larger unimodal size distribution. Such phenomena can be justified in terms of the variation in the frameworks growth rate. Here one needs to carefully bear in mind that the MOF growth processes being driven by the diffusion of monomers from solution to the framework surfaces, a considerable large increase in the dimensions of these frameworks results in an increase in the thickness of their boundary layers,[37] thereby suppressing the diffusion of monomers and limiting the attachments associated with the

**1306** | *Mater. Chem. Front.*, 2019, **3**, 1302–1309

This journal is © The Royal Society of Chemistry and the Chinese Chemical Society 2019
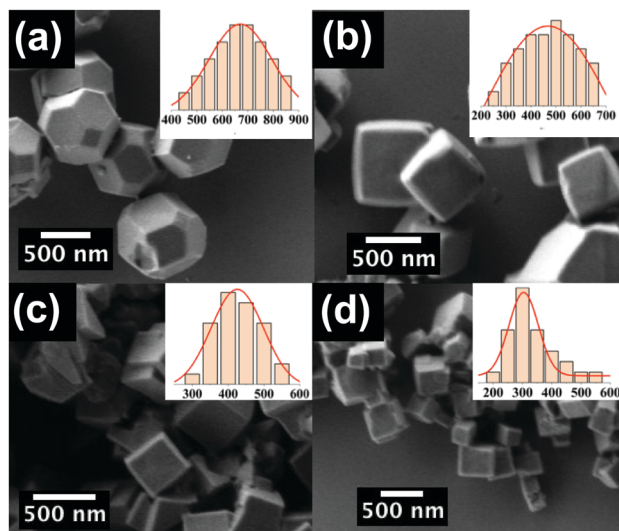
**Fig. 5** SEM micrographs along framework size distribution for the synthesis carried out at 25 °C using 5 min ablation time and (a) 10, (b) 20, (c) 30 and (d) 40 mg cm$^{-3}$ of Hmim.

growth processes. To this end, one can rationalize that the growth rates for a given MOF population will decay as the frameworks become larger. Therefore, it is not hard to imagine that if sufficient monomers are available in the solution, the smaller MOFs will grow at a faster rate while the growth rates of the larger frameworks will decrease eventually such that all the MOF species will tend to reach similar dimensions over significantly long time scales and lead to a unimodal size distribution. Ideally, detailed investigations for actual observation and explanation of the aforementioned mechanistic picture would involve *in situ* probing into the system to map out the population size distributions in real-time – a measurement that would be valuable yet highly involved, and beyond the scope of our current experimental set-up.

**Effect of the synthesis temperature**

In our effort to investigate the influence of synthesis temperatures on the LASiS-based MOF fabrications, here we analyze the formation of the frameworks under the identical set of experimental conditions as before, but for a different synthesis temperature. We study the final MOF products for different Hmim concentrations using 5 min as the ablation time, while maintaining the system at 25 °C. The results, (observed from the inset size distributions as indicated in Fig. 5) show a gradual decrease in the average framework sizes as the concentration of Hmim increases.

These findings also corroborate our results obtained in the previous sections for the synthesis carried out at 65 °C. However, when carefully inspected, the products formed at lower temperature (25 °C) show larger average framework sizes when compared to the sizes obtained for the same set of previous experimental conditions at the higher temperature (65 °C). These observations clearly support the strong temperature dependence of the nucleation rates, and, as discussed earlier, a higher nucleation rate yields greater number of MOF structures with lower average sizes. The results at the lower temperature LASiS also indicate a

distinct change in the MOF morphologies with increasing linker Hmim concentrations. Thus, for the lowest Hmim concentration, the MOF frameworks generate a truncated rhombic dodecahedron morphology with {100} and {110} faces expressed (Fig. 5a). On the other hand, as the Hmim concentration increased, the frameworks exhibit progressively smaller cubic morphologies with the {100} faces expressed (Fig. 5b–d). The synthesis temperature can modify the attachment energy and hence, the rates of attachment during crystallization, which in turn, have a strong relationship to the morphology of the final crystal structure. This morphological control of the frameworks presents a remarkable advantage for MOF synthesis. It becomes immediately apparent that by adjusting the morphology it is possible to modify the orientation of the pore apertures and functional groups, thereby regulating their accessibility and hence, the degree of interaction with the species of interest.

## 4. Conclusions

We have presented here a systematic study of LASiS-based synthesis of MOF structures, specifically using ZIF-67 as the model MOF system. Our results provide fundamental insights into the mechanistic roles of solution-phase parameters and laser properties, heretofore not investigated in detail for laser-induced MOF formation routes. Specifically, we proposed a sequence of reaction pathways during the LASiS technique that is initiated by high-energy laser-driven ablation of a metal target resulting in the nucleation of metal NPs that subsequently undergo solution-phase oxidation to generate Co$^{2+}$ ions. The large population of the metal ions coordinates with active sites on the Hmim molecules in the solution-phase that is immediately followed by the Hmim deprotonation resulting in the final MOF crystal nucleation, and subsequent oligomerization processes originating the growth phenomena. The organic linker to metal ion stoichiometric ratio, as controlled by the initial Hmim concentrations and ablation time for the LASiS technique, have been shown to bear substantial influence on the sizes of the framework. These results indicate that a higher Hmim concentration under a given laser ablation time yielded MOFs with smaller average sizes, while an increase in the ablation time using a constant Hmim concentration produced structures with larger average sizes. These findings have been rationalized based on the deprotonation rates; specifically, a higher Hmim to Co$^{2+}$ stoichiometric ratio accelerates the Hmim deprotonation, inducing enhanced nucleation rates. We hypothesize that the enhancement in the nucleation rate is achieved at the expense of the framework sizes formed, while bearing in mind that most of the Hmim/Co centers participate in the formation of new nuclei and only a limited amount of material contributes to the growth of existing MOF structures. We also investigated the role of the synthesis temperature during the LASiS process on the MOF formations. Our results indicate that the MOF morphology can be tailored by optimizing the temperature for a given set of experimental parameters during LASiS *via* modulating the attachment energy and rates of attachment during the MOF crystallization

process. In summary, the present study lays the groundwork for LASiS as a facile, green and efficient technique for the rational design and synthesis of a wide library of diverse MOF structures in future.

## Conflicts of interest

There are no conflicts to declare.

## Acknowledgements

## References

1 G. Ferey, Hybrid porous solids: past, present, future, *Chem. Soc. Rev.*, 2008, **37**(1), 191–214.

2 V. Stavila, A. A. Talin and M. Allendorf, MOF-based electronic and opto-electronic devices, *Chem. Soc. Rev.*, 2014, **43**(16), 5994–6010.

3 O. K. Farha, I. Eryazici, N. C. Jeong, B. G. Hauser, C. E. Wilmer, A. A. Sarjeant, R. Q. Snurr, S. T. Nguyen, A. O. Z. R. Yazaydın and J. T. Hupp, Metal–organic framework materials with ultrahigh surface areas: is the sky the limit?, *J. Am. Chem. Soc.*, 2012, **134**(36), 15016–15021.

4 H. Furukawa, N. Ko, Y. B. Go, N. Aratani, S. B. Choi, E. Choi, A. Ö. Yazaydin, R. Q. Snurr, M. O'Keeffe and J. Kim, Ultrahigh porosity in metal-organic frameworks, *Science*, 2010, **329**(5990), 424–428.

5 H. Furukawa, K. E. Cordova, M. O'Keeffe and O. M. Yaghi, The chemistry and applications of metal-organic frameworks, *Science*, 2013, **341**(6149), 1230444.

6 H. Furukawa and O. M. Yaghi, Storage of hydrogen, methane, and carbon dioxide in highly porous covalent organic frameworks for clean energy applications, *J. Am. Chem. Soc.*, 2009, **131**(25), 8875–8883.

7 D. Farrusseng, *Metal–organic frameworks: applications from catalysis to gas storage*, John Wiley & Sons, 2011.

8 S.-L. Li and Q. Xu, Metal–organic frameworks as platforms for clean energy, *Energy Environ. Sci.*, 2013, **6**(6), 1656.

9 D. Farrusseng, S. Aguado and C. Pinel, Metal–organic frameworks: opportunities for catalysis, *Angew. Chem., Int. Ed.*, 2009, **48**(41), 7502–7513.

10 J. Heine and K. Müller-Buschbaum, Engineering metal-based luminescence in coordination polymers and metal–organic frameworks, *Chem. Soc. Rev.*, 2013, **42**(24), 9232–9242.

11 M. C. So, G. P. Wiederrecht, J. E. Mondloch, J. T. Hupp and O. K. Farha, Metal–organic framework materials for light-harvesting and energy transfer, *Chem. Commun.*, 2015, **51**(17), 3501–3510.

12 B. Chen, Z. Yang, Y. Zhu and Y. Xia, Zeolitic imidazolate framework materials: recent progress in synthesis and applications, *J. Mater. Chem. A*, 2014, **2**(40), 16811–16831.

13 J. Cravillon, R. Nayuk, S. Springer, A. Feldhoff, K. Huber and M. Wiebcke, Controlling Zeolitic Imidazolate Framework Nano- and Microcrystal Formation: Insight into Crystal Growth by Time-Resolved In Situ Static Light Scattering, *Chem. Mater.*, 2011, **23**(8), 2130–2141.

14 J. A. Thompson, C. R. Blad, N. A. Brunelli, M. E. Lydon, R. P. Lively, C. W. Jones and S. Nair, Hybrid Zeolitic Imidazolate Frameworks: Controlling Framework Porosity and Functionality by Mixed-Linker Synthesis, *Chem. Mater.*, 2012, **24**(10), 1930–1936.

15 K. S. Park, Z. Ni, A. P. Cote, J. Y. Choi, R. Huang, F. J. Uribe-Romo, H. K. Chae, M. O'Keeffe and O. M. Yaghi, Exceptional chemical and thermal stability of zeolitic imidazolate frameworks, *Proc. Natl. Acad. Sci. U. S. A.*, 2006, **103**(27), 10186–10191.

16 K. Kida, M. Okita, K. Fujita, S. Tanaka and Y. Miyake, Formation of high crystalline ZIF-8 in an aqueous solution, *CrystEngComm*, 2013, **15**(9), 1794–1801.

17 R. Wagia, I. Strashnov, M. W. Anderson and M. P. Attfield, Insight and Control of the Crystal Growth of Zeolitic Imidazolate Framework ZIF-67 by Atomic Force Microscopy and Mass Spectrometry, *Cryst. Growth Des.*, 2018, **18**(2), 695–700.

18 Q. Bao, Y. Lou, T. Xing and J. Chen, Rapid synthesis of zeolitic imidazolate framework-8 (ZIF-8) in aqueous solution via microwave irradiation, *Inorg. Chem. Commun.*, 2013, **37**, 170–173.

19 N. Stock and S. Biswas, Synthesis of metal-organic frameworks (MOFs): routes to various MOF topologies, morphologies, and composites, *Chem. Rev.*, 2012, **112**(2), 933–969.

20 T. Friščić, Metal-Organic Frameworks: Mechanochemical Synthesis Strategies, *Encyclopedia of Inorganic and Bioinorganic Chemistry*, 2014, pp. 1–19.

21 S. Hu, C. Melton and D. Mukherjee, A facile route for the synthesis of nanostructured oxides and hydroxides of cobalt using laser ablation synthesis in solution (LASIS), *Phys. Chem. Chem. Phys.*, 2014, **16**(43), 24034–24044.

22 S. Hu, K. M. Cheng, E. L. Ribeiro, K. Park, B. Khomami and D. Mukherjee, A facile and surfactant-free route for nanomanufacturing of tailored ternary nanoalloys as superior oxygen reduction reaction electrocatalysts, *Catal. Sci. Technol.*, 2017, **7**(10), 2074–2086.

23 D. Mukherjee and S. Hu, Compositions, Systems and Methods for Producing Nanoalloys, and/or Nanocomposites using tandem Laser Ablation Synthesis in Solution-Galvanic Replacement Reaction, *US Pat.*, 15/132,916, 2017.

24 S. Hu, M. Tian, E. L. Ribeiro, G. Duscher and D. Mukherjee, Tandem laser ablation synthesis in solution-galvanic replacement reaction (LASiS-GRR) for the production of PtCo nanoalloys as oxygen reduction electrocatalysts, *J. Power Sources*, 2016, **306**, 413–423.

25 S. Hu, G. Goenaga, C. Melton, T. A. Zawodzinski and D. Mukherjee, PtCo/CoOx nanocomposites: Bifunctional electrocatalysts for oxygen reduction and evolution reactions synthesized via tandem laser ablation synthesis in solution-galvanic replacement reactions, *Appl. Catal., B*, 2016, **182**, 286–296.

26 S. A. Davari, S. Hu, E. L. Ribeiro and D. Mukherjee, Rapid elemental composition analysis of intermetallic ternary nanoalloys using calibration-free quantitative Laser Induced Breakdown Spectroscopy (LIBS), *MRS Adv.*, 2017, 1–6.

27 S. A. Davari, S. Hu and D. Mukherjee, Calibration-free quantitative analysis of elemental ratios in intermetallic nanoalloys and nanocomposites using Laser Induced Breakdown Spectroscopy (LIBS), *Talanta*, 2017, **164**, 330–340.

28 S. Hu, E. L. Ribeiro, S. A. Davari, M. K. Tian, D. Mukherjee and B. Khomami, Hybrid nanocomposites of nanostructured Co3O4 interfaced with reduced/nitrogen-doped graphene oxides for selective improvements in electrocatalytic and/or super-capacitive properties, *RSC Adv.*, 2017, **7**(53), 33166–33176.

29 S. A. Davari, J. L. Gottfried, C. Liu, E. L. Ribeiro, G. Duscher and D. Mukherjee, Graphitic coated Al nanoparticles manu-factured as superior energetic materials via laser ablation synthesis in organic solvents, *Appl. Surf. Sci.*, 2019, **473**, 156–163.

30 V. Amendola and M. Meneghetti, What controls the compo-sition and the structure of nanomaterials generated by laser ablation in liquid solution?, *Phys. Chem. Chem. Phys.*, 2013, **15**(9), 3027–3046.

31 G. Lu, S. Li, Z. Guo, O. K. Farha, B. G. Hauser, X. Qi, Y. Wang, X. Wang, S. Han, X. Liu, J. S. DuChene, H. Zhang, Q. Zhang, X. Chen, J. Ma, S. C. Loo, W. D. Wei, Y. Yang, J. T. Hupp and F. Huo, Imparting functionality to a metal-organic framework material by controlled nanoparticle encapsulation, *Nat. Chem.*, 2012, **4**(4), 310–316.

32 Z. Ozturk, M. Filez and B. M. Weckhuysen, Decoding Nucleation and Growth of Zeolitic Imidazolate Framework Thin Films with Atomic Force Microscopy and Vibrational Spectroscopy, *Chemistry*, 2017, **23**(45), 10915–10924.

33 D. Saliba, M. Ammar, M. Rammal, M. Al-Ghoul and M. Hmadeh, Crystal Growth of ZIF-8, ZIF-67, and Their Mixed-Metal Derivatives, *J. Am. Chem. Soc.*, 2018, **140**(5), 1812–1823.

34 V. K. LaMer and R. H. Dinegar, Theory, Production and Mechanism of Formation of Monodispersed Hydrosols, *J. Am. Chem. Soc.*, 1950, **72**, 4847–4854.

35 V. K. LaMer, Nucleation in Phase Transitions, *Ind. Eng. Chem.*, 1952, **44**, 1270–1277.

36 S. A. Davari and D. Mukherjee, Kinetic Monte Carlo simulation for homogeneous nucleation of metal nanoparticles during vapor phase synthesis, *AIChE J.*, 2018, **64**, 18–28, DOI: 10.1002/aic.15887.

37 T. Sugimoto, F. Shiba, T. Sekiguchi and H. Itoh, Spontaneous Nucleation of Monodisperse Silver Halide Particles from Homogeneous Gelatin Solution I: Silver Chloride, *Colloids Surf., A*, 2000, **164**, 183–203.

38 D. B. K. Chu, J. S. Owen and B. Peters, Nucleation and Growth Kinetics from LaMer Burst Data, *J. Phys. Chem. A*, 2017, **121**(40), 7511–7517.

This journal is © The Royal Society of Chemistry and the Chinese Chemical Society 2019

*Mater. Chem. Front.*, 2019, **3**, 1302–1309 | **1309**